J Mater Sci (2011) 46:5977–5990
DOI 10.1007/s10853-011-5559-8

# Density and plastic strain evaluations using small-angle X-ray scattering and finite element simulations for powder compacts of complex shape

**L. H. Han · P. R. Laity · R. E. Cameron · J. A. Elliott**

Received: 16 January 2011 / Accepted: 11 April 2011 / Published online: 22 April 2011


**Abstract** Previous work suggested that two-dimensional small-angle X-ray scattering (2D-SAXS) could offer a new method for evaluating the local variations of density, strain and principal strain direction within powder compacts, which arise due to the effects of friction and die shape. In order to test this method further, this work compared results from 2D-SAXS with finite element (FE) simulations using a modified density-dependent Drucker–Prager Cap (DPC) model, for compacts of complex shape, prepared using a cylindrical die, a flat-faced upper punch and shaped lower punches with three different central protrusions. Variations in compaction behaviour were observed, which were due to friction against the die walls and the punch shape. Good agreement was obtained between SAXS measurements and FE simulation, supporting previous indications. Hence, this combination of experimental and computational techniques appeared particularly powerful for investigating powder compaction behaviour, in considerable accuracy and detail. Moreover, observations of the compaction behaviour in the vicinity of the central protrusion may be relevant to tablets with embossed features or compacted artefacts of more complex shape.

L. H. Han
Department of Computer Science, University College London, Gower Street, London WC1E 6BT, UK

P. R. Laity (✉)
School of Applied Sciences, University of Huddersfield, Queensgate, Huddersfield HD1 3DH, UK
e-mail: p.laity@hud.ac.uk

R. E. Cameron · J. A. Elliott
Department of Materials Science and Metallurgy, University of Cambridge, New Museums Site, Pembroke St., Cambridge CB2 3QZ, UK

## Introduction

The pharmaceutical industries depend heavily on compacted tablet formulations. This, in addition to various other engineering applications, makes a good understanding of powder compaction behaviour of paramount importance. Recent studies of various compacted powders [1–4] demonstrated that their two-dimensional small-angle X-ray scattering (2D-SAXS) patterns became elongated in the compaction direction, to an extent that increased with the applied upper punch pressure. This suggested a potential method for studying compaction behaviour, based on an empirical relationship between the changes in 2D-SAXS and relative density ($\rho_{rel}$, i.e. bulk density divided by true density). Analysis of data from different locations across diametral cross-section revealed variations in $\rho_{rel}$, along with local changes in compaction direction, which were attributable to the effects of friction against the compaction die and punch shapes. Subsequent work suggested a more quantitative relationship, based on deformation of the nanometre scale morphology within granules (herein referred to as nano-strain) during compaction. Although this effect may vary significantly between individual granules, it was shown that the aggregated effect over a large number of granules was equivalent to initially spherical elements of volume being compressed along the direction of applied stress, into ellipsoids [3]. This appeared to involve a volume reduction during compression (i.e. affine deformation of the nano-scale intragranular morphology, qualitatively similar to the uniaxial compaction of the bulk powder bed), which was probably facilitated by voids in the sub-granular structure [5] collapsing.

The effects of wall friction on the distribution of forces within a granular bed have been known for a considerable time, following the first scientific analysis by Janssen

[6, 7]. Moreover, the widespread importance of powder compaction, in situations as diverse as grain silos, civil engineering and the manufacture of products from metal, ceramic or polymeric powders, has stimulated an enormous body of work. Indeed, the importance of compacted tablets for pharmaceutical dosage forms alone has driven much of this work.

A considerable range of experimental methods have been employed to investigate powder compaction, including force–displacement measurements, helium pycnometry, mercury intrusion porosimetry, indentation measurements of hardness and various types of microscopy. Several recent studies [8–10] used X-ray microtomography (XμT) to observe local density variations within tablets. Eiliazadeh et al. [11] used XμT to follow the movements of metal shot tracer beads, to investigate the effect of die geometry on the compaction behaviour of a pharmaceutical excipient powder. Djemai and Sinka [12] also demonstrated the use of magnetic resonance imaging with a non-swelling, permeating liquid to observe density distributions within tablets of differing shapes and preparation conditions.

In parallel with experimental investigations, there have been considerable advances in the modelling of powder compaction [9, 13, 14], including significant work by Cunningham, Sinka and Zavaliangos [15–17], Hassanpour and co-workers [18, 19] and Michrafy et al. [20, 21], amongst others [22–28]. These simulations fall into two categories: discrete model and continuum model methods. The former treat each powder particle individually and analyse the contact interactions and deformation of the particles, while the continuum model methods consider the powder as a continuous elasto-plastic medium. While discrete model methods are more useful for understanding the physical processes of powder compaction, they present computational difficulties in simulating large-scale plastic deformations of powders [29]. Although a powder is clearly discontinuous at the particle level, this becomes less relevant at a larger scale of aggregation, such as when it is compacted to a relatively high density in a die, during tabletting. Therefore, continuum model methods, with phenomenological models based on the principles of continuum mechanics at a macroscopic level, have been widely used for studying the compaction behaviour of powders in metallurgical, ceramic, pharmaceutical and other fields. A continuum model method has been used in this study, where a modified density-dependent Drucker–Prager Cap (DPC) plasticity model [9, 28] was implemented in a commercial finite element (FE) package (ABAQUS), to simulate powder compaction behaviour.

SAXS is a well established and widely used method for conducting morphological studies [30, 31]. Since the scattering arises due to the interactions of X-rays with electrons, SAXS is sensitive to electron density variations associated with morphological features over the scale of roughly 1–100 nm. The versatility of SAXS has led to numerous publications in many diverse fields of science and engineering; nevertheless, its application to investigating powder compaction has emerged only recently [1–4].

Initial work [1, 2] studied the effects of compaction on pre-gelatinised starch, spheronised microcrystalline cellulose (s-MCC) and hydroxypropyl-methyl-cellulose, materials commonly used as pharmaceutical excipients for compacted tablets. Empirical relationships were demonstrated between the applied punch pressure, $\rho_{rel}$ and changes in the 2D-SAXS patterns for a series of flat-faced cylindrical specimens. Subsequent work [3] proposed an explanation for the observed changes in 2D-SAXS patterns, based on affine deformation and volume reduction of the 'fractal-like' sub-granular structures of the powders [5] during compaction (i.e. qualitatively similar to the behaviour of the macroscopic powder bed). This led to the concept of 'nano-strain' of the sub-granular morphology on the nanometre scale during compaction, as a contribution to but distinct from the overall 'macro-strain' of the powder bed, which also included the mechanisms of granule movement and fragmentation. In a recent paper [4] the SAXS method was used to reveal variations in the compaction behaviour within tablets of different size and shape. As an extension of that work, this investigation used 2D-SAXS to estimate both density and strain distributions within powder compacts of more complex shape, comparing the results with simulations using FE methods. In addition to providing a rigorous test of both the SAXS and FE methods, the results are expected to be a stepping stone towards subsequent investigations into more challenging applications such as sintered engineering parts and compacted artefacts with irregular shapes, including pharmaceutical tablets with grooves, company logos or other embossed features.

## Experimental methods

### Specimen preparation

Specimens for SAXS experiments were prepared using s-MCC powders (Celphere SCP100, Asahi-Kasei, Japan, stored under ambient conditions and used as received). Fractionation by sieving found 90% by weight of this material had granule sizes between 75 and 212 μm, in line with the manufacturer's product description. Single-sided, uniaxial compaction was performed in a stainless steel die (nominally 10 mm internal diameter, Specac Ltd. Smiths Industries, Kent, UK), with a driven upper punch and static

lower punch. Specimens of different shapes were produced using a shaped lower punch (manufactured at the Department of Materials Science and Metallurgy, University of Cambridge), incorporating a central cylindrical, hemispherical or conical protrusion, with dimensions as shown in Table 1.

Compaction experiments were performed using an Instron 5567 mechanical testing apparatus (Instron Ltd. High Wycombe, Buckinghamshire, UK), at a speed of 3 mm $min^{-1}$, during both loading and unloading stages, as described previously [1, 2]. Once the maximum loading (nominally 15 kN, equivalent to an average upper punch pressure of 191 MPa) was reached, unloading followed immediately. The displacement and force were recorded during each compaction experiment, in order to calculate curves showing average upper punch pressure versus relative density. Each specimen was ejected from the die immediately after unloading, in the same direction as the compression. Diameter ($d$) and height ($h$) were measured using callipers with a vernier scale (to ±0.02 mm), within about 1 min after ejection; the mass ($m$) was subsequently measured using an electronic top-pan balance (to ±0.0003 g). Results are shown in Table 1.

The dimensions of the specimens were further checked by XμT using a 1072 bench-top tomograph (Skyscan, Belgium) at a magnification of ×22 (giving a pixel size of 12.74 μm), in order to generate geometrical models for FE simulations. The sealed microbeam X-ray source was set at 46 kV, 224 μA and a 0.5 mm aluminium filter was used. The specimens were individually mounted (upside-down) on a Perspex rod, using double-sided adhesive tape. A series of projections were collected at (nominally) 0.45° steps from 0° to 180°, using an exposure time of 7.5 s per frame and a 4-frame average at each step. Reconstruction of the tomographic data was performed using N-Recon software (Skyscan, Belgium) and the resulting stacks of images were subsequently analysed using Image-J software (available from the NIH, [32]). Images of diametral sections, as shown in Fig. 1, were prepared by 're-slicing' regions of interest spanning 10 voxels (i.e. cubic volumetric equivalent of square pixels) either side of the diameter, then projecting the average grayscale (and adding false colour for digital publication).

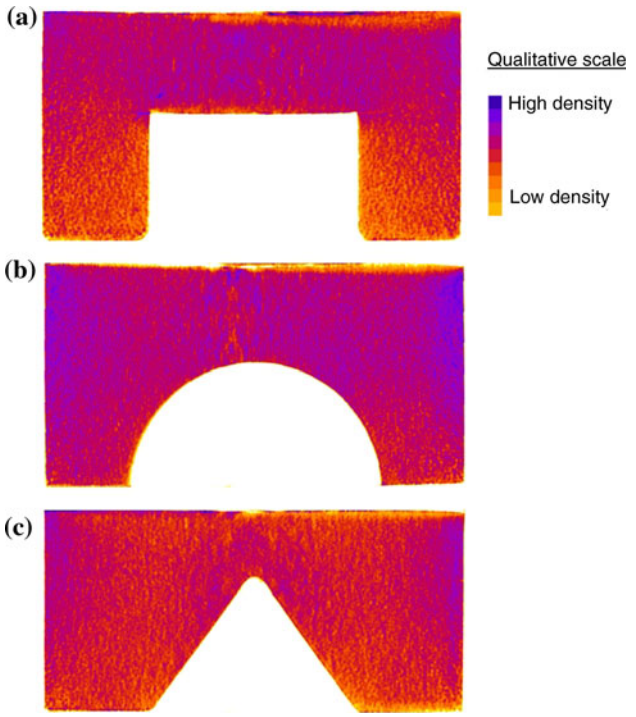


**Fig. 1** Images of diametral sections from XμT, showing (qualitative) variations in density, for specimens made using: **a** cylindrical, **b** hemispherical and **c** conical protrusions (false colour applied for improved clarity in the digital publication)

## SAXS measurements

Detailed descriptions of the methods used to collect and analyse the SAXS data are presented elsewhere [1–4], so only the main points are summarised here.

2D-SAXS data were collected using a Nanostar camera (Bruker AXS Inc. Madison, WI, USA), with Cu Kα radiation (wavelength, $\lambda_X = 0.154$ nm) and a gas-filled wire-grid 'Hi-star' detector. A sample-to-detector distance of (nominally) 1.06 m was used, which was calibrated using the scattering from silver behenate. The entire beam-path, including sample chamber, was evacuated to minimise air scattering. A lead beam-stop was suspended in front of the detector, to protect it from the intense beam of undeviated X-rays.

Compacted specimens were shaved using a sharp scalpel, to prepare diametral sections roughly 2 mm thick.

**Table 1** Experimental details and simulation parameters for specimens made with different protrusions

| Protrusion | | | | Experimental specimens | | | | Simulated filling height (mm) |
|---|---|---|---|---|---|---|---|---|
| Shape | Radius (mm) | Height (mm) | Volume ($mm^3$) | Weight (g) | Height (mm) | Diameter (mm) | Average $\rho_{rel}$ | |
| Cylindrical | 2.5 | 3.0 | 58.9 | 0.5065 | 5.54 | 10.02 | 0.845 | 10.04 |
| Hemispherical | 3.0 | 3.0 | 56.6 | 0.5006 | 5.30 | 10.02 | 0.874 | 9.90 |
| Conical | 2.5 | 3.0 | 19.6 | 0.5113 | 4.92 | 10.02 | 0.876 | 9.63 |

Specimens of this thickness produced strong scattering patterns, while minimising any effects due to surface damage during preparation. Sections were individually attached to the computer-controlled sample stage within the SAXS apparatus, which was programmed to raster the X-ray spot over the specimen. The spot size was about 0.9 mm, albeit with the highest intensity close to the centre, which limited the spatial resolution with the present apparatus to roughly 0.5 mm. Consequently, the spot was moved in increments of 0.5 mm, both horizontally and vertically. (It may be noted, however, that finer resolution would be possible, using apparatus with a smaller X-ray spot size.)

Acquisition times of 900 s were used at each location across the specimen. Background scattering was found to be negligible, under these conditions; therefore, correction was considered unnecessary. Intensity curves were extracted from the 2D-SAXS patterns using SAXS for Windows® NT software (Bruker AXS Inc. Madison, WI, USA). Examples of the changes in 2D-SAXS data from different locations on a diametral section (for a specimen prepared using a cylindrical protrusion) are shown in Fig. 2.

## Analysis of SAXS data

The analysis used azimuthal variations (i.e. intensity changes around the direction of the incident beam), which were measured by scanning around the 2D-SAXS patterns in steps of $d\phi = 0.5°$, over an angular range that included all the observable scattered intensity. The results were quantified using the Hermans orientation parameter ($H$) defined as [30]:

$$H = \frac{3\langle \cos^2 \phi \rangle - 1}{2} \tag{1}$$

where

$$\langle \cos^2 \phi \rangle = \frac{\int_0^{360} I(\phi) \cos^2 \phi \cdot |\sin \phi| \cdot d\phi}{\int_0^{360} I(\phi) \cdot |\sin \phi| \cdot d\phi} \tag{2}$$

The integration in Eq. 2 was performed numerically, using Microsoft® Excel®. Use of $|\sin \phi|$ avoided the change of sign at 180°, allowing the integration to be performed between 0° and 360° and giving better accuracy. Hence, it was generally possible to determine $H$ to ±0.003.

The overall scattered intensity depended on X-ray absorbance, which was affected by specimen thickness and density; indeed, absorbance was used previously to reveal (qualitative) local density variations within a cross-section [2]. Variations in X-ray absorbance (due to thickness or density variations) did not significantly affect $H$ or the subsequent analyses, however. Consequently, the results appeared to be essentially unaffected by specimen preparation—although care was still taken to prepare reasonably uniform cross-sections.

Deviations between the major axis of the 2D-SAXS pattern and the vertical (i.e. the direction of applied force) were evaluated by substituting:

$$\phi = \phi_L + \kappa \tag{3}$$

where $\phi_L$ is the azimuthal angle, measured from the vertical direction in the 'laboratory frame' and searching for the value of $\kappa$ that maximised $H$, using the 'Solver' subroutine in Excel.

## Relative density estimates

Relative density (i.e. bulk density divided by true density, where $\rho_{true} = 1590$ kg m$^{-3}$ [9]) was estimated from SAXS data, using the calibration reported previously for s-MCC [2], which is described by the equation:

$$\rho_{rel} = 0.433 + 0.411H + 0.449\left[1 - \exp\left\{-\frac{H}{0.008}\right\}\right] \tag{4}$$

This relationship is also shown in Fig. 3a. Although related to the compaction behaviour of s-MCC, depending on the balance between deformation within the subgranular nanometre scale morphology and the overall compaction of the powder bed, Eq. 4 is essentially empirical.

Uncertainty in the values of relative density from Eq. 4 arose in two ways: at low densities, it was mainly attributable to the errors in measuring $H$ (±0.003); this improved at higher densities, but was limited by the variability in the relative densities (±0.02) of the calibration samples used to obtain the relationship. Hence, the uncertainty was estimated to be ±0.05 at $\rho_{rel} = 0.77$, decreasing to ±0.02 for $\rho_{rel} \geq 0.85$ and less than ±0.01 for $\rho_{rel} \geq 0.90$.

## Nano-strain of granules

Previous work [3] suggested that the changes in 2D-SAXS patterns observed for compacted powder were due to deformation of the 'fractal-like' nanometre scale intragranular morphology [5] (herein referred to as 'nano-strain'). On that basis, a relationship between nano-strain and the Hermans orientation parameter for s-MCC was obtained, which is described by:

$$\varepsilon_{nano} = 2.9006H - 1.1104H^2 \tag{5}$$

where a positive value of $\varepsilon_{nano}$ indicates compression. This relationship is also shown in Fig. 3b. The uncertainty of ±0.003 in obtaining $H$ corresponded to an uncertainty of ±0.009 in the values of $\varepsilon_{nano}$.

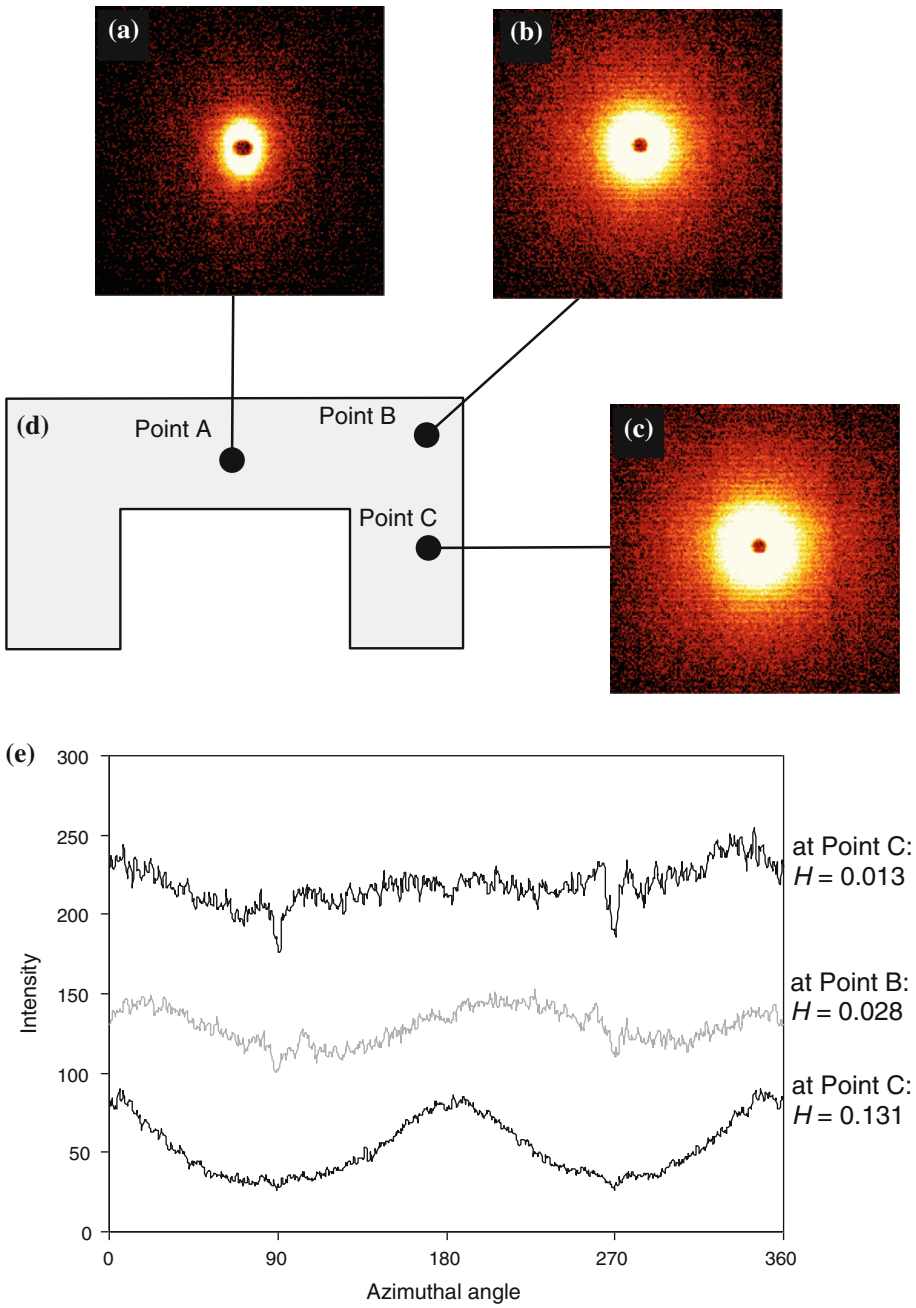


**Fig. 2** Typical SAXS data, at three different positions, from a specimen made using a cylindrical protrusion: **a–c** examples of 2D-SAXS patterns; **d** showing approximate locations where SAXS data (*Points A–C*) were collected; **e** azimuthal plots corresponding to the SAXS patterns in **a–c**

## FE simulation

The entire compaction process, including ejection, was simulated for the three different profiled lower punches, using the FE method. A modified density-dependent DPC plasticity model was implemented in ABAQUS version 6.7 (Dassault Systèmes, France) [33], in line with previous publications [9, 15–17, 20–23, 28]. Changes in mechanical properties of the powder bed with density during compaction were accommodated using tabulated parameters and a user-defined subroutine.

### FE parameterisation for Celphere SCP100

Several FE simulations of microcrystalline cellulose compaction have been reported previously [15–17, 20, 22, 23, 28], but those studies used Avicel, rather than spheronised Celphere SCP100. Although these materials are chemically similar, the compaction behaviour may also be affected by the granule shape and internal morphology. Consequently, it was necessary to obtain a parameterisation describing the s-MCC used in the experimental part of this study.

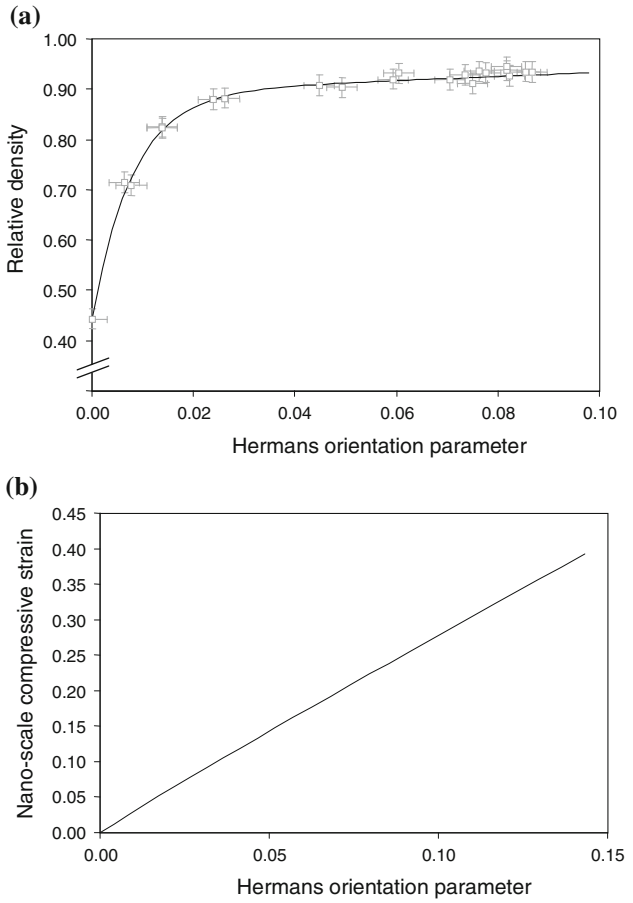


**Fig. 3** Calibration functions for estimating **a** relative density and **b** nano-strain from SAXS measurements

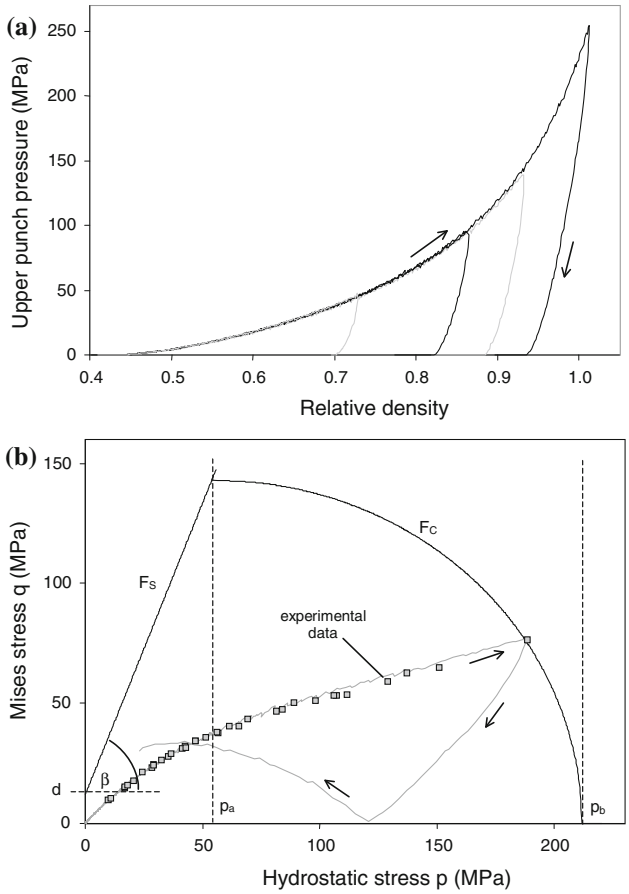


**Fig. 4** Selected data sets from compaction simulator, used to obtain FE parameterisation: **a** upper punch pressure versus relative density; **b** DPC model and compaction behaviour in *p*–*q* space, *filled squares* show maximum pressure points from individual experiments

The FE parameter set for Celphere SCP100 was measured following the methods reported previously [9, 15, 28]. Flat-faced cylindrical specimens were prepared using a hydraulic compaction simulator fitted with an instrumented die, which was lubricated by painting the walls using a suspension of magnesium stearate in ethanol. After calibrating the punch separation (using a 8 mm thick slip gauge), the lower punch was retracted and the powder charge added manually. The upper punch moved at 0.1 mm $s^{-1}$, during compaction and subsequent unloading, while the forces on both punches and the stress at the die wall were recorded. After unloading, the upper punch was retracted and the lower punch moved upwards (also at 0.1 mm $s^{-1}$) to eject the specimen, which was promptly measured and weighed, in order to calculate the relative density. By adjusting the powder charge (0.226–0.287 g) and the expected minimum punch separation (3.40–4.75 mm), maximum punch pressures in the range 17–255 MPa were obtained; this achieved values of $\rho_{rel}$ in the range 0.594–1.015 at maximum loading, which gave specimens with $\rho_{rel}$ in the range 0.572–0.897 after ejection. Four typical compaction experiments to different target densities are compared in Fig. 4a; the concurrence of the loading curves demonstrates the excellent agreement between data sets.

Analysis of the compaction data using Janssen–Walker theory gave values of the friction coefficient ($\mu$) for s-MCC against the lubricated die wall in the range 0.05–0.11. This variation in $\mu$ between compaction experiments was probably due to how thoroughly the magnesium stearate lubricant suspension had been painted onto the tooling. Young's modulus ($E$) and Poisson's ratio ($v$) were obtained from the wall stress and punch pressures during the unloading phase of each experiment, following the methods described previously by Han et al. [28], which assumed a non-linear elastic unloading behaviour.

The key features of the DPC model are plotted in the *p*–*q* plane in Fig. 4b, where $p$ is the hydrostatic stress and $q$ is the Mises equivalent stress, as described elsewhere [9, 15, 28]. For the cylindrical symmetry in this work, these can be calculated as:

$$p = -\frac{(\sigma_z + 2\sigma_r)}{3} \tag{6a}$$

$$q = |\sigma_z - \sigma_r| \tag{6b}$$

The meanings of the various parameters describing the DPC model are shown diagrammatically in Fig. 4b. The position of the shear failure surface ($F_S$), in terms of its slope ($\beta$) and intercept ($d$), was calculated from the axial and diametral breaking strengths of the compacted specimens after ejection, as described elsewhere [15, 28]. Other DPC model parameters describing the cap surface ($F_C$) in terms of its ellipticity ($R$) and the $p$-co-ordinates ($p_a$ and $p_b$) of the intersections with $F_S$ and the $p$-axis, were subsequently obtained from peak pressure measurements, following the methods described previously by Han et al. [28]. In order to achieve a smooth transition between $F_S$ and $F_C$, a transition surface was included in the model and an empirical constant ($\alpha = 0.02$) was used, in line with previous work [28].

Examples of experimental compaction data in $p$–$q$ space are also plotted in Fig. 4b. Again, the excellent reproducibility is demonstrated by the maximum pressure points from different compaction experiments all falling very close to the curve representing the compaction data for the highest pressure run achieved in this work. The small deviations between experiments may be attributed to variations in wall friction, due to how thoroughly the die was lubricated.

In order to minimise experimental uncertainty, trend lines were fitted through the results obtained for each parameter over the range of relative densities achieved. Thus, empirical equations describing the dependences of the various parameters were obtained, from which the values shown in Table 2 were calculated.

## FE compaction simulation for Celphere SCP100

Axisymmetric models were employed, consistent with the geometry and constraints expected in the experimental compaction set-up. Geometric models and mesh configurations for simulating compactions with the three shaped lower punches are shown in Fig. 5. Each model consisted of two rigid punches, a rigid die and a deformable powder bed. Both the upper punch and die had the same radius (5.00 mm); the dimensions of the three lower punches in the geometrical models were as shown in Fig. 5. The simulated powder charges matched the weights of the experimental specimens, giving the initial filling heights ($h_0$) shown in Table 1, based on a filling density ($\rho_{fill}$) of 694 kg m$^{-3}$ (corresponding to $\rho_{rel} = 0.438$).

The rigid punch and die were modelled as analytical rigid bodies; the powder bed was modelled using axisymmetric continuum elements and elements of the CAX4R type, comprised of a network of 4-node quadrilaterals, each with a single integration point and 'hourglass control'. In order to avoid severe distortion of some elements due to the large strains involved in the compaction process, a 'mesh-to-mesh solution mapping' re-meshing technique was used, as provided in ABAQUS/Standard. This replaced the deformed mesh with a mesh of better quality, before continuing the simulation. Contacts between the powder and the rigid tooling were modelled by defining contact pairs of surfaces. The tooling surface was associated with a rigid body by its specified reference node, on which the loads or displacement of a rigid body were applied. Frictional contact between surfaces was simulated using the Coulomb friction law. For s-MCC against non-lubricated tooling, a wall friction coefficient of $\mu = 0.2$ was applied, based on previous work [28]. For comparison, simulations were also performed for zero wall friction.

The simulations included three steps, representing compression, decompression and ejection, respectively. In the first step, the upper punch head was moved downwards by applying a displacement to its reference point, to simulate the compression process, while the die and the lower punch remain fixed. In the second step (representing decompression), the upper punch was moved out of the die by applying an upward displacement to its reference point. In the third step, the lower punch was moved upwards against the powder compact, representing ejection of the tablet from the die. For the sake of simplicity, the third step could also be simulated by releasing all the contact forces between powders and the die set, in the following way: first, all the displacements of a compact within a die were frozen to their current state (i.e. after unloading) by applying a displacement boundary condition; then, all the contacts were removed by disabling the mechanical interaction between contact surfaces; finally, the displacement boundary defined in the previous step was removed, to allow free recovery of the simulated compact.

The relative density and principal plastic strain direction after ejection were calculated through a user-defined subroutine. Relative density was calculated from the volumetric plastic strain ($\varepsilon_v^p$) through the relationship:

$$\varepsilon_v^p = \varepsilon_{xx} + \varepsilon_{yy} + \varepsilon_{zz} = \ln\left\{\frac{\rho_{rel}}{\rho_0}\right\} \tag{7}$$

where a positive value indicates compression, $\varepsilon_{xx}$, $\varepsilon_{yy}$ and $\varepsilon_{zz}$ are the normal strains calculated in the radial (i.e. horizontal), axial (i.e. vertical) and circumferential directions and $\rho_0$ is the initial relative density, corresponding to the filling density. The principal plastic strain direction was determined from the total strain tensor, $\boldsymbol{\varepsilon}$, as:

**Table 2** FE parameterisation for Celphere SCP100

| Relative density | Poisson's ratio $\nu$ | Young's modulus $E$ (MPa) | Slope $\beta$ (°) | Intercept $d$ (MPa) | Cap ellipticity $R$ | $p_b$ (MPa) |
|---|---|---|---|---|---|---|
| 0.44 | 0.140 | 56.31 | 70.1 | 0.0523 | 0.506 | 0.26 |
| 0.45 | 0.142 | 268.40 | 70.0 | 0.0612 | 0.529 | 0.79 |
| 0.50 | 0.153 | 499.18 | 69.9 | 0.1281 | 0.623 | 4.66 |
| 0.55 | 0.164 | 585.30 | 69.7 | 0.2498 | 0.687 | 8.24 |
| 0.60 | 0.177 | 798.25 | 69.5 | 0.4598 | 0.731 | 17.20 |
| 0.65 | 0.190 | 987.71 | 69.3 | 0.8060 | 0.766 | 25.46 |
| 0.70 | 0.204 | 1191.14 | 69.1 | 1.3552 | 0.804 | 37.68 |
| 0.75 | 0.211 | 1403.35 | 68.8 | 2.1984 | 0.854 | 55.76 |
| 0.80 | 0.221 | 1664.33 | 68.6 | 3.4566 | 0.929 | 74.19 |
| 0.85 | 0.224 | 2006.97 | 68.4 | 5.2876 | 1.038 | 111.12 |
| 0.88 | 0.228 | 2252.46 | 68.2 | 6.7435 | 1.125 | 162.01 |
| 0.90 | 0.235 | 2563.49 | 68.1 | 7.8944 | 1.193 | 190.73 |
| 0.92 | 0.241 | 3250.76 | 68.0 | 9.2098 | 1.270 | 231.42 |
| 0.95 | 0.246 | 4023.33 | 67.9 | 11.5336 | 1.404 | 287.48 |
| 0.98 | 0.267 | 4862.15 | 67.7 | 14.3430 | 1.563 | 338.40 |
| 1.00 | 0.285 | 5475.86 | 67.6 | 16.5258 | 1.683 | 395.85 |

$$\theta_p = 0.5 \tan^{-1}\left(\frac{2\varepsilon_{xy}}{\varepsilon_{xx} - \varepsilon_{yy}}\right) \quad (8)$$

where $\theta_p$ denotes the angle between the horizontal direction ($x$-axis) and the direction of the principal strain and $\varepsilon_{xy}$ is the shear strain.

## Results and discussion

In order to check the reliability of the FE parameter set, five powder compaction experiments were chosen at random, over the range of maximum pressures achieved and their compaction curves simulated using the weights and minimum punch separations listed in Table 3. The comparisons between the FE simulations and the experimental data are shown in Fig. 6. In each case, the simulated loading curves and maximum pressure points matched the experimental data very well. Slightly larger discrepancies were evident during unloading, particularly for the higher pressure runs, where the simulations did not reproduce the non-linear behaviour of the experimental specimens. This was not surprising since unloading elicits elasto-plastic recovery; in this work, the compacted specimens exhibited further density decreases during ejection and subsequent storage. Nevertheless, even in the worst case (Expt. 5), the simulated $\rho_{\text{rel}}$ was within 0.02 of the experimental result for the fully unloaded specimen in the compaction die. Thus, it appeared that the FE simulations using the parameters obtained here closely matched the compaction behaviour of the s-MCC used for the experiments.

XμT images of the diametral sections from the three specimens are shown in Fig. 1, where the colour gives a qualitative indication of density variations. The data were slightly degraded by electronic 'noise' of high spatial frequency. Regions of lighter colour were also observed across the top of each cross-section; these were imaging artefacts associated with the mountings used to support the specimens. Nevertheless, higher density rims were observable around the upper part of each compact, where the greatest effect of wall friction was expected, while low density regions were indicated in the lower part, around the protrusion. A large region of high density was also indicated above the cylindrical protrusion, while smaller variations were associated with the hemispherical and conical protrusions.

Typical SAXS data from three different locations across the specimen made using the cylindrical protrusion are presented in Fig. 2. The data at Point A, above the cylindrical protrusion, showed the strongest azimuthal variation ($H = 0.131$), indicating the greatest local compaction and relative density. This also resulted in the lowest overall intensity, due to X-ray absorbance by the s-MCC. The smallest azimuthal variations were found to the sides of the cylindrical protrusion, as exemplified by the data at Point C. In this case, the low relative density resulted in weaker X-ray absorbance and stronger overall intensity; nevertheless, the azimuthal variation was only just discernible above the random 'noise' in the data. Slight dips in the intensity were also evident close to 90°, 180°, 270° and 360°, due to the absorbance of X-rays by the polymeric filaments used to support the beam-stop. The azimuthal

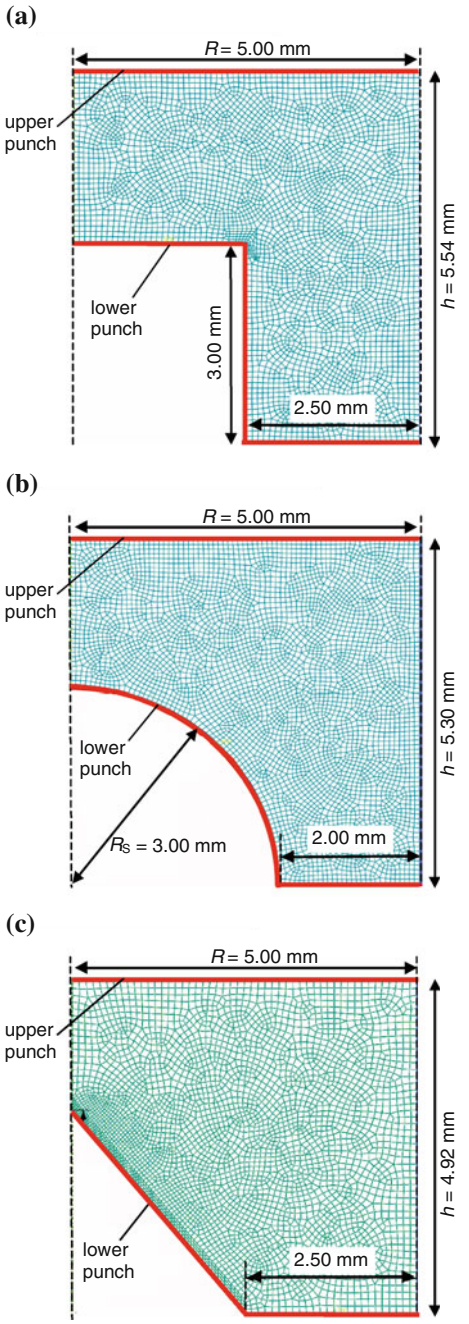


**Fig. 5** Typical mesh and geometry of FE models for specimens made using: **a** cylindrical, **b** hemispherical and **c** conical protrusions

variation at Point B showed a small angular off-set; the two maxima were located close to 30° and 210°, which was attributable to the effect of wall friction on the resultant compaction force at that location. By performing similar analyses at all the locations across each diametral section, it was possible to construct maps of SAXS data, from which estimates of relative density, nano-strain and principal strain direction were obtained.

Relative density estimates from SAXS (i) are compared with FE predictions with and without wall friction

**Table 3** Experimental parameters for compaction tests used to validate the extracted DPC model parameters

| Experiment number | 1 | 2 | 3 | 4 | 5 |
|---|---|---|---|---|---|
| Powder weights (g) | 0.2269 | 0.2302 | 0.2315 | 0.2781 | 0.2866 |
| Minimum punch separation (mm) | 4.770 | 3.946 | 3.457 | 3.713 | 3.553 |

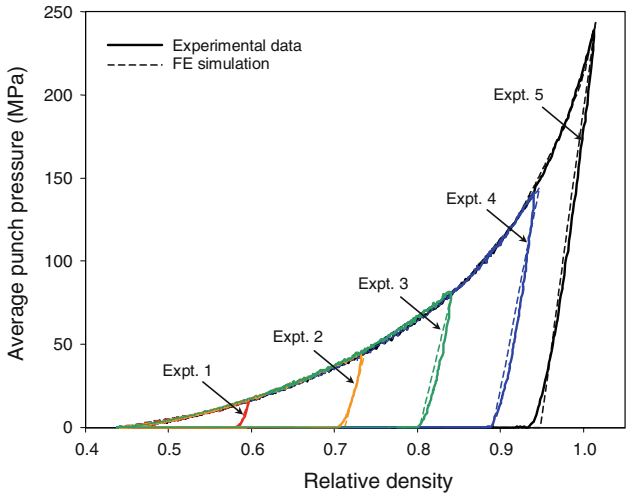


**Fig. 6** Comparison between measured punch pressure and predicted values from FE model

(ii and iii), in the form of colour-coded maps of the diametral sections for each protrusion shape, in Fig. 7. Only one half of each diametral section is shown, since the compacted specimens were expected to exhibit cylindrical symmetry. This allowed SAXS measurements to be made across both sides of the diametral section, then averaged to give the results shown. The continuous lines roughly indicate the outlines of the specimens. Due to the finite size of the X-ray spot on the sample (about 0.9 mm diameter), 2D-SAXS patterns collected close to the outer edges of the specimens were contaminated by strong reflection spikes, which prevented reliable analysis. Hence, there was a gap between the experimental results and the specimen outline. This limitation did not apply to the 'inside edges' adjacent to the protrusion, however, due to the finite thickness of the specimen and curvature of this surface. Although the FE simulation did not incur the same limitations, it was decided to omit the outermost results, in order to facilitate comparisons with the SAXS data. Also, although the FE method was capable of predictions at a much higher spatial resolution (depending on the element size and the computing power required to run the model), the results were locally averaged to match the same spatial resolution (0.5 mm) as the SAXS results.

Good agreement was found between the results from SAXS analysis, using Eq. 4, and the FE simulation with

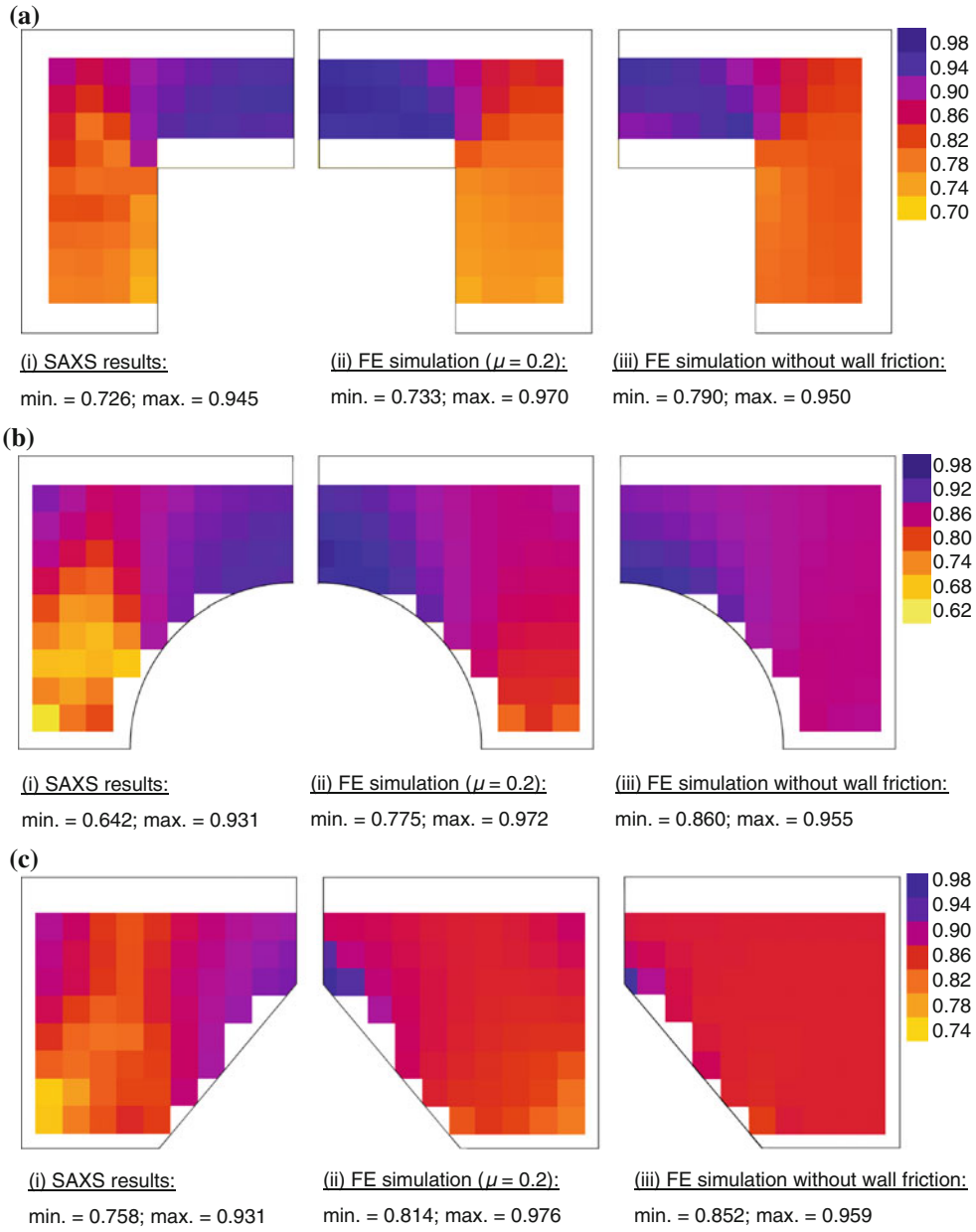


**Fig. 7** Comparison between relative density results from SAXS and FE simulations (with and without wall friction, $\mu$) for specimens made using: **a** cylindrical, **b** hemispherical and **c** conical protrusions; *the solid lines* represent the edges of the cross-sections (maps shown in colour in the digital version)

wall friction ($\mu = 0.2$), in terms of both the numerical ranges and distribution patterns of the relative densities, for each of the protrusion shapes. Generally, the differences between the two methods amounted to little more than the experimental uncertainties in average density and SAXS measurements.

Moreover, the results in Fig. 7 matched the qualitative density variations shown by the XμT images in Fig. 1—albeit with considerably less interference by electronic 'noise'. In each case, the relative densities decreased down the sides of the specimen, from the upper to lower rim; this can be attributed to the effect of wall friction and was absent from the simulations with no wall friction. A region of very high density (i.e. higher density than the upper rim) was also observed within each specimens, just above the top of the central protrusion from the lower punch. This effect appeared most pronounced for the cylindrical protrusion, in terms of its extent and the density range, while the conical protrusion produced the smallest effect. These high density regions remained in the FE simulations, even in the absence of wall friction. Similar high density regions, associated with moulded break-lines across tablets, have also been reported by Sinka and co-workers [10, 12].

Variations in strain within the cross-sections, estimated from SAXS data and predicted by FE simulation, are compared in Fig. 8. In each case, a positive value indicates compression. Arrows are also superimposed over the colour-coded maps, indicating local variations in the principal

strain direction, which were obtained from the principal axis of the 2D-SAXS patterns, using Eqs. 1–3, or from the total plastic strain tensor in the FE simulations, using Eq. 8 and allowing for the thickness of the experimental specimens. Note: true strain values from FE simulations are shown in Fig. 8, for an easier understanding of how much the powder has been compressed.

The nano-strain obtained from SAXS data using Eq. 5 was considerably smaller than the principal compressive strain indicated by FE simulation. This was mainly due to the different meanings of the quantities calculated. The nano-strain was associated only with deformation of the intragranular morphology that occurred during the compaction process [3, 4]; other compaction mechanisms, involving granule movement or fragmentation, which contributed to the macro-strain of the powder bed were excluded from the nano-strain. By contrast, the FE method treated the powder bed as a compressible continuum, so that the strain results predicted by this method included granule rearrangement and fragmentation, which are believed to dominate the early stage of compaction. It was demonstrated previously [3, 4] that the relationship between macro- and nanostrain is highly non-linear, with the former dominating the low density compaction stage, while the latter increased dramatically for $\rho_{rel} > 0.6$. It may be noted that random close packing of uniform spheres gives a relative density of around 0.64 [34, 35]. Although higher densities can be achieved by polydispersed spheres or non-spherical particles, it seems likely that this would represent a reasonable estimate for the onset of more extensive granule deformation. On this basis, compaction from $\rho_{rel} = 0.438$ (starting point for FE

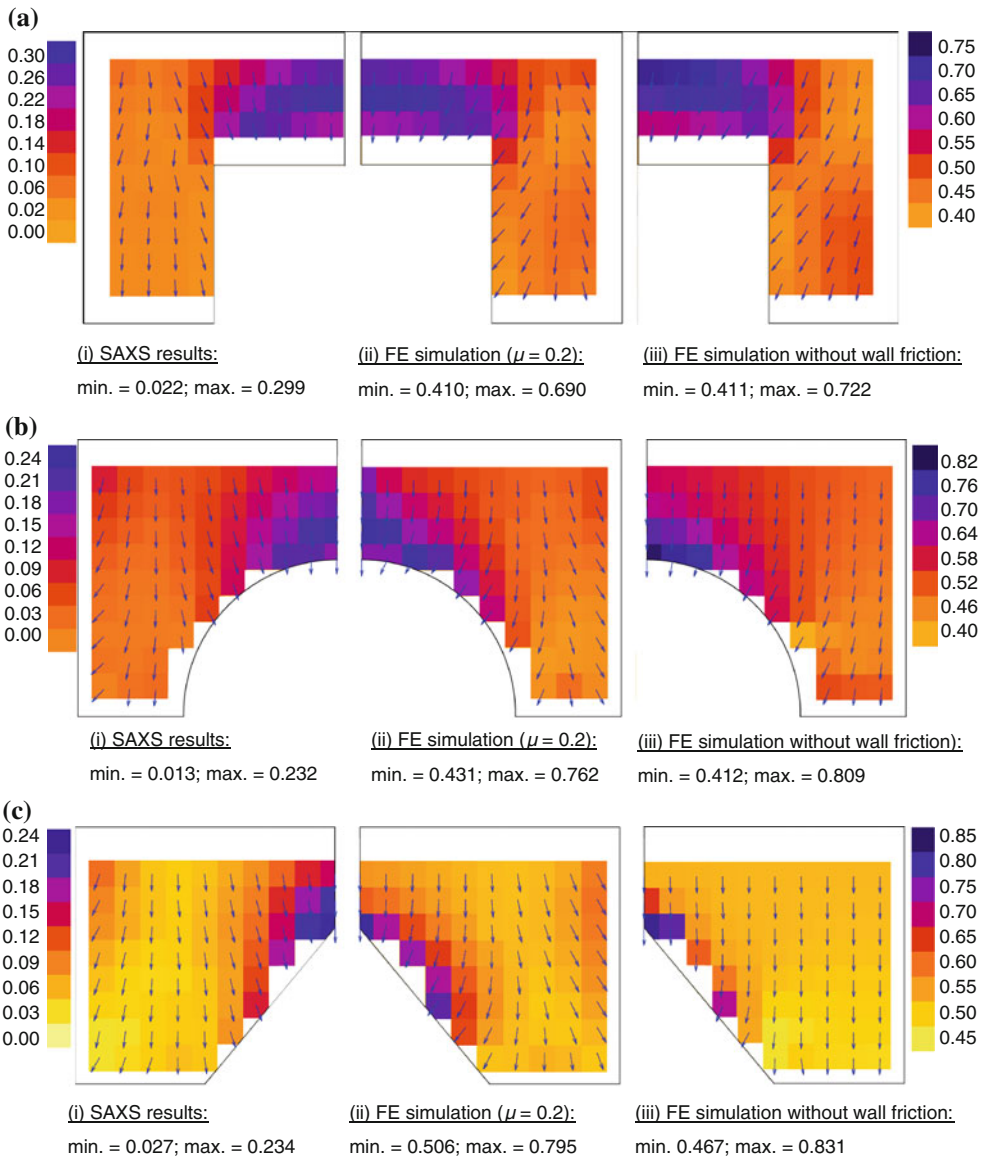


**Fig. 8** Comparison between nano-strain from SAXS and principal strains from FE simulations (with and without wall friction, $\mu$) for specimens made using: **a** cylindrical, **b** hemispherical and **c** conical protrusions; *arrows* illustrate the principle strain direction (maps shown in colour in the digital version)

simulations) to $\rho_{rel} = 0.6$ (onset of granule deformation associated with significant nanostrain) corresponded to an engineering strain of 0.37.

Finally, it should be noted the comparison is made with the principal compressive strain calculated in the FE simulation. For 'normal' powder compactions in a cylindrical die, using flat-faced punches, the compression occurs close to the axial direction, so that principal strain is roughly the same as volumetric strain. In this work, however, the use of the shaped lower punch could cause significant outward (radial) movement and some tensile (i.e. extensional) strain. For example, at one point in the compaction using the die with the cylindrical protrusion:

$\varepsilon_{11} = 0.133$ (i.e. compressive in the radial direction),
$\varepsilon_{22} = 1.918$ (i.e. compressive in the axial direction),
$\varepsilon_{33} = -0.471$ (i.e. extensional in the circumferential direction),
$\varepsilon_{12} = 1.953$ (i.e. compressive in the shear direction),
$\varepsilon_{max} = 2.348$ (i.e. compressive principal strain),
$\varepsilon_v^p = 1.580$ (i.e. compressive volumetric strain)

Nevertheless, in spite of the differences in numerical values, the patterns of qualitative variations in nano-strain from SAXS results and principal strain from FE simulations (with $\mu = 0.2$) appeared very similar.

It may be noted that values of 'bulk' compressive macro-strain can also be obtained from the relative densities calculated using SAXS data. These were closer to the FE strain predictions. This comparison is not shown, however, since it effectively reiterates the relative density comparison of Fig. 7.

In general, good agreement was also observed between the principal strain directions from SAXS and FE simulation (with $\mu = 0.2$), as indicated by the arrows. The largest discrepancies coincided with the lowest values of $H$ (and $\varepsilon_{nano}$); this was to be expected, since it was relatively difficult to determine the principal axis of almost circularly symmetric 2D-SAXS data. There appeared to be significant outward strain components close to the sides of the diametral sections, where the powder was in contact with die surfaces; hence the arrows appeared to lean inwards, towards the centre of the specimen. This may be attributed to wall friction, since it was absent from the FE simulations with frictionless die walls. Additional changes in strain direction were also observed due to the central protrusion from the lower punch.

While the methods demonstrated here are very capable of revealing variations in relative density (and the corresponding bulk compressive strain) within powder compacts, similar information can also be obtained by other means, such as XμT [8–10] or MRI [12]. Conversely, it is very difficult to obtain information concerning local variations in principal strain direction using other methods, although it may be possible by following the precise movements of tracer particles [11]. Moreover, the authors are not aware of any other methods that could quantify the nano-strain deformation of granules and the macro-strain of the powder bed separately, which emphasises the potential offered by SAXS studies of powder compaction.

One further observation deserves a brief comment: preparing diametral sections revealed dark regions within the specimens, suggesting that the s-MCC had been scorched during compaction. This was most pronounced with the cylindrical protrusion, as shown in Fig. 9a, although close examination also revealed faint discoloration with the hemispherical and conical protrusions. While this interpretation is presently conjectural (and further investigation is currently underway), scorching suggested a significant temperature rise. The location inside the compact appeared to preclude any significant contribution from wall friction. Instead, it appeared to be due to energy dissipation by friction between granules or granules undergoing deformation during compaction. Significantly, the greatest discoloration appeared to coincide with the region of highest density, which had experienced the greatest compaction strain, as demonstrated by comparison with the FE simulation in Fig. 9b.

It is widely known that industrial powder compaction can cause considerable tablet heating. Despite its potential importance, however, this phenomenon has attracted only limited scientific investigation [36–41]. The main contribution to heating is believed to be from irreversible mechanical work of compaction, in the form of friction between granules, friction against tooling surfaces and plastic deformation of granules. The surface energy of the system may also decrease, due to the expected reduction of surface area within or between powder granules during compaction; however, this is expected to be several orders of magnitude smaller than the contribution from mechanical work. On this basis, Zavaliangos et al. predicted temperatures in the region of 30–55 °C for flat-faced, cylindrical [36] and capsule-shaped [37] MCC tablets produced under various compaction conditions, which appeared to agree with their experimental measurements using an infrared camera. It seems likely that even higher temperatures would have occurred in the high density regions caused by the shaped lower punches used in this work.

The present observations of apparent 'hot-spots' inside the compacts suggest that, at least in some circumstances, energy dissipated by granule deformation or friction between granules may be more important than friction against the tooling. For example, the use of tooling to produce artefacts of complex shape may concentrate the

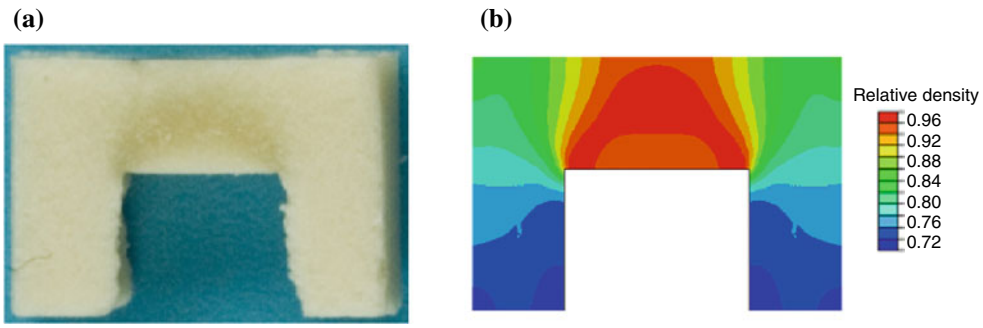


**Fig. 9** Observation of scorching within a cross-section prepared using the lower punch with the cylindrical protrusion: **a** visual appearance; **b** FE simulated density distribution

heating effects inside the compact. These issues will be the subject of further work, to be reported separately. It should be noted that the density-dependent DPC model used in this work did not attempt to simulate temperature changes. Moreover, it was assumed that the materials properties were not affected by any temperature change associated with the compaction process. Incorporating the interdependent aspects of heat generation during compaction affecting materials properties is not a trivial extension of the present DPC model; while ABAQUS can easily accommodate temperature-dependent mechanical parameters, apparatus for measuring those dependences during compaction is not readily available. Consequently, the expected temperature-dependences of key mechanical properties (such as $p_a$, $p_b$, $E$ and $\mu$) have been ignored in recent publications [36, 37]. This is probably acceptable for simulating compaction close to room temperature, but may not be realistic for larger temperature increases, whether due to incremental changes over successive compactions (as observed during prolonged industrial manufacturing runs) or resulting from more extreme mechanical work dissipation (as hypothesised in the present case). These issues will be considered in further work.

It should also be noted that the present experiments and simulations were performed at much slower compaction speeds than commercial compaction processes. While this should not affect the amounts of energy involved, it does allow more time for heat conduction. Hence, any temperature rise may be more pronounced at commercial pressing rates.

## Conclusions

As an extension of our previous experimental study on powder compaction, SAXS was used to evaluate the plastic strain and the relative density of three powder compacts with more complicated shapes. To better understand the SAXS results, they were compared with predictions from FE simulations using a modified density-dependent DPC plasticity model for powder compaction.

Results from the two methods were in good agreement, with respect to local variations in relative density and the principal directions of compaction strain within compacts. Moreover, the nano-strain distribution from SAXS exhibited qualitatively similar patterns to the principal plastic strain distribution from FE simulations, even though the values were quantitatively different. This difference can be explained because the former measured the deformation of the intragranular morphology (nano-strain) while FE simulations provided the total deformation (macro-strain) of the powder beds.

It appeared that SAXS was able to determine both the magnitude and net direction of the compaction strain without the need for tracer particles or coloured layers. This presents significant advantages over other methods for investigating powder compaction, including local hardness, X-ray absorbance or pore volume-fraction measurements. The FE method based on a modified DPC model for powders also provided quantitative predictions concerning the density and plastic strain distributions of powder compacts. The method developed here, combining SAXS measurements with FE simulations, is highly applicable for the study of powder compaction, particularly for pharmaceutical materials.

Moreover, the compaction behaviour observed in the vicinity of the central die protrusions provides insight into the effects of local shape variations. Although the spatial resolution in this work was limited to 0.5 mm, consistent with the X-ray spot size of the apparatus used, finer resolution would be possible in both the simulations and experimental measurements. In the case of the FE method, this is limited only by the size of the elements used and the computing power required to run the model. Finer resolution could also be achieved in the SAXS method, using a smaller spot size—including the possibility of a 'microbeam' at a synchrotron source. Hence, this work provides a stepping stone towards subsequent investigations into more challenging applications, such as the use of tooling to produce artefacts of complex shape, including embossed company logos or break-lines on tablet surfaces.

**Acknowledgements** This work was supported by Pfizer Ltd. who also provided access to a compaction simulator with an instrumented die, which was used to obtain the FE parameterisation. The authors are grateful to Yuen Sin Cheong and Craig Bentham, at Pfizer Ltd.

Sandwich, UK for their help in performing the compaction simulation experiments.

## References


1. Laity PR, Cameron RE (2008) Powder Technol 188:119
2. Laity PR, Cameron RE (2009) Powder Technol 192:287
3. Laity PR, Cameron RE (2010) Powder Technol 198:404
4. Laity PR, Han LH, Elliott JA, Cameron RE (2010) J Pharm Sci 99:4380
5. Laity PR, Cassidy AMC, Skepper J, Jones W, Cameron RE (2010) Eur J Pharm Biopharm 74:377
6. Sperl M (2006) Granular Matter 8:59
7. Pitman EB (1998) Phys Rev E 57:3170
8. Busignies V, Leclerc B, Porion P, Evesque P, Courraze G, Tchoreloff P (2006) Eur J Pharm Biopharm 64:38
9. Wu C-Y, Ruddy OM, Bentham AC, Hancock BC, Best SM, Elliott JA (2005) Powder Technol 152:107
10. Sinka IC, Burch SF, Tweed JH, Cunningham JC (2004) Int J Pharm 271:215
11. Eiliazadeh B, Pitt K, Briscoe B (2004) Int J Solid Struct 41:5967
12. Djemai A, Sinka IC (2006) Int J Pharm 319:55
13. Brewin P, Coube O, Doremus P, Tweed JH (2007) Modelling of powder die compaction. Springer Publishing Co., New York
14. Kremer DM, Hancock BC (2006) J Pharm Sci 95:517
15. Cunningham JC, Sinka IC, Zavaliangos A (2004) J Pharm Sci 93:2022
16. Sinka IC, Cunningham JC, Zavaliangos A (2003) Powder Technol 133:33
17. Sinka IC, Cunningham JC, Zavaliangos A (2004) J Pharm Sci 93:2040
18. Samimi A, Hassanpour A, Ghadiri M (2005) Chem Eng Sci 60:3993
19. Hassanpour A, Ghadiri M (2004) Powder Technol 141:251
20. Michrafy A, Dodds JA, Kadiri MS (2004) Powder Technol 148:53
21. Michrafy A, Ringenbacher D, Tchorelof P (2002) Powder Technol 127:257
22. Sinha T, Bharadwaj R, Curtis JS, Hancock BC, Wassgren C (2010) Powder Technol 202:46
23. Sinha T, Curtis JS, Hancock BC, Wassgren C (2010) Powder Technol 198:315
24. Picker KM (2000) Eur J Pharm Biopharm 49:267
25. Sonnergaard JM (1999) Int J Pharm 193:63
26. Lordi NG, Cocolas H, Yamasaki H (1997) Powder Technol 90:173
27. Skrinjar O, Larsson P-L, Storåkers B (2007) Trans ASME 74:164
28. Han LH, Elliott JA, Bentham AC, Mills A, Amidon GE, Hancock BC (2008) Int J Solids Struct 45:3088
29. Dutt M, Hancock BC, Bentham AC, Elliott JA (2005) Comput Phys Commun 166:26
30. Roe R-J (2000) Methods of X-ray and neutron scattering in polymer science. Oxford University Press, New York
31. Higgins JS, Stein RS (1978) J Appl Cryst 11:346
32. More information on Image-J and software downloads are available at: http://rsbweb.nih.gov/ij/
33. ABAQUS 6.7 documentation, ABAQUS Inc. 2007
34. Mehta A (2007) Granular physics. Cambridge University Press, Cambridge (with contributions from Sir Sam Edwards, Blumenfeld R, Goldhirsch I, Claudin P)
35. Zallen R (1998) The physics of amorphous solids. Wiley, New Yok
36. Zavaliangos A, Galen S, Cunningham J, Winstead D (2008) J Pharm Sci 97:3291
37. Klinzing GR, Zavaliangos A, Cunningham J, Mascaro T, Winstead D (2010) Comput Chem Eng 34:1082
38. Bechard SR, Down GRB (1992) Pharm Res 9:521
39. Ketolainen J, Ilkka J, Paronen P (1993) Int J Pharm 92:157
40. Wurster DE, Rowlings CE, Creekmore JR (1995) Int J Pharm 116:179
41. Buckner IS, Friedman RA, Wurster DE (2010) J Pharm Sci 99:861